Research Article | Vol. 27, No. 23 / 11 November 2019 / Optics Express 33925
Optics EXPRESS

Highly multiplexed Bragg gratings for large field of view gas sensing in planetary atmospheres

S. Y. Haffert,* E. H. Por, and C. U. Keller

Leiden Observatory, Leiden University, PO Box 9513, Niels Bohrweg 2, 2300 RA Leiden, The Netherlands
*haffert@strw.leidenuniv.nl

Abstract: Detecting and monitoring gas species is an important part of remote sensing because the state of the environment can be retrieved from the state of the gas species. This can be used to track temperature and pressure structures in the atmosphere for weather predictions, or monitor the air quality. Discriminating different species is easier at higher spectral resolution when the spectral lines are clearly resolved. The need to do this at high spatial resolution and over large fields of view leads to a trade-off between spectral and spatial resolution and spectral bandwidth. We propose to use a highly multiplexed Bragg grating that can optically combine the relevant information from the spectrum without the need to disperse the whole spectrum. This allows us to circumvent the spatial and spectral trade-off and therefore substantially increase the field of view compared to conventional hyperspectral imagers. A dynamic implementation based on acousto-optical filters that can be adapted on the fly is discussed as an easy and flexible way to create the multiplexed gratings. We describe the details of multiplexed Bragg gratings and show that we can retrieve the spatial distribution of individual species abundances in gas mixtures, and we show that we can even do this for the atmospheres of exoplanets orbiting far-away stars.

1. Introduction

Hyperspectral imaging is a corner stone of modern remote sensing. An important application is the monitoring of gases in the atmosphere, especially in urban areas where air pollution can be a serious health problem [1]. Gas tracing is also done in industrial settings for the detection and monitoring of hazardous emissions from large industrial facilities [2,3], finding leaks in large gas pipes or the indoor formation of gases during production processes. Nowadays we also observe the atmospheres of other planets, even planets around stars other than our own Sun. In all these cases it is important to know where, when, which and how much gas is present. A sensor that is built to remotely detect these gases will need to be able to spatially and spectrally resolve the spectral absorption lines of these gases.

Gases have a specific spectral signature that is created by their atomic or molecular structure. These signatures become more distinct from each other at higher spectral resolution. An example can be seen in Fig. 1, where high-resolution transmission spectra of various molecules are generated with HAPY [4], the python interface of HITRAN2012 [5]. In the selected wavelength range methane shows a set of strong, distinct spectral lines that are quite different from the signatures of CO_2 and water. The difference is even more extreme compared to O_2, which does not have any features in this spectral range. By measuring the spectral information we can exploit the differences in spectral signatures between gases to classify and monitor them from a distance.

The presence of a molecular species in a spectrum can be found by using a matched spectral filter [6] that is tuned to the signature of the species of interest. A simple matched filter can be made with a binary mask that is equal to one where a spectral line is present and zero otherwise. Because most spectral lines of interest are absorption lines, the binary matched filter (BMF) will have a low signal when all the lines are present, as there is less flux inside the absorption line. On the other hand if the spectral lines are not present the signal will be high as there is no absorption.

#370083 https://doi.org/10.1364/OE.27.033925
Journal © 2019 Received 14 Jun 2019; revised 20 Sep 2019; accepted 22 Sep 2019; published 6 Nov 2019

Optics EXPRESS

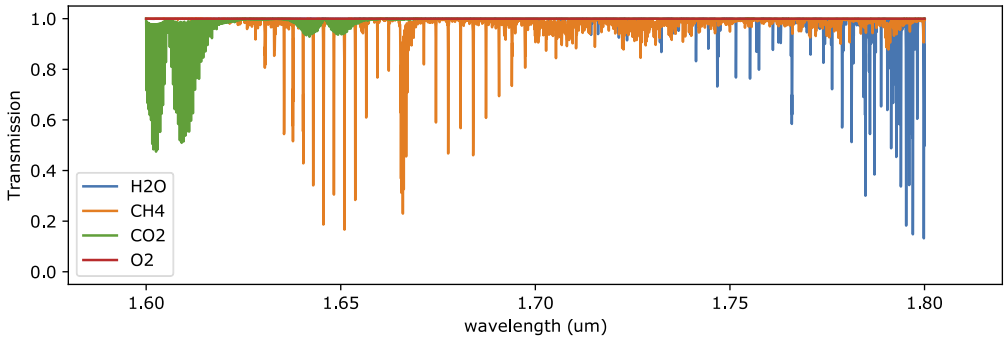

Fig. 1. The spectra of water, methane and carbon-dioxide are shown in the wavelength range from 1.6 to 1.8 μm. Each spectrum consists of many sharp spectral lines, but due to the amount and close proximity of the spectral lines, these can merge and form an absorption band, which can be seen as the shaded areas. The different molecules have distinct spectral features at high spectral resolution.

For moving objects it is important to take the Doppler shift into account, which shifts the position of spectral lines. If the Doppler shift is neglected, it could lead to a miss-classification because the species is present but shifted. Small shifts can be accounted for by cross-correlating the measured spectrum with the matched filter. This has been successfully used in astronomy to look for very weak signatures of molecular species in the atmospheres of extra-solar planets that are buried in the light of their host star [7–9]. For a clear detection of several gases it is important to have high-spectral resolving power, but a high-resolution spectrum for every point in the field-of-view is very costly in terms of detector real estate. Therefore most conventional hyperspectral imagers need to compromise between spatial and spectral resolving power.

An alternative way of measuring gases is by using a gas-filter correlation sensor [3,8]. Here the light passes through a gas-cell that is filled with the species of gas that needs to be detected. If light of interest passes through a gascell containing methane, for example, the absorption features of methane will be imprinted in the light. Suppose that the light already had the lines of methane imprinted in it, because it passed through some clouds of methane in the Earth's atmosphere, then the total amount of light will not change much because all light that could have been absorbed by the methane in the gas-cell is already gone. If the light did not have the imprints of methane, the total intensity will decrease because light is lost due to the absorption by methane. Therefore if we pass the light through two gas cells, one containing methane and one empty reference cell, the ratio in intensity between the two will correlate with the presence of methane. This mimics the behaviour of a binary matched spectral filter. The gas-cell correlation method allows for a large field of view as the correlation signal can be recorded with only two pixels. A downside of the gas-cell sensor is its ability to only measure species with vanishing relative Doppler shift. If the input is Doppler-shifted, the absorption lines do not align anymore with the absorption lines of the gas-cell sensor, and the differential measurement will no longer detect the species.

For some species it may to be possible to create a solution that is purely optical and does not need gas cells. An example is the HIGS sensor that has been developed for NO_2 measurements [10]. HIGS replaces the gas-cell correlation with an all-optical filter. HIGS uses an interferometer that has periodic fringes to create a matched spectral filter, which matches the periodic spectral lines of NO_2. Another example are the OH-suppression fiber Bragg gratings [11]. These are used to remove the atmospheric OH emission lines to decrease the amount of contamination they have on the astronomical spectrum of interest. While these methods may decrease the number of pixels, they lose precious information because the line shapes are sensitive to temperature, pressure, velocity and molecular abundance variations. With careful monitoring of the spectral

Optics EXPRESS

lines of interest it is possible to retrieve these parameters. But approaches like the gas-cell sensor or the HIGS lose this information as they reduce the full spectrum to a single intensity difference and therefore can only measure the abundance of the molecule.

In this work we present a dynamic, eletro-optical solution based on highly multiplexed acousto-optical volume Bragg gratings (HMBG), which can do the same measurement as gas-cell sensors but retain the spectral line shape information. The HMBG are also very flexible as it is possible to electronically switch the spectral filter. In Section 2 we discuss the principles of a Bragg grating and its multiplexing capabilities that are relevant for trace-gas measurements. In section 3 we highlight the advantages of the HMBG. In section 4 we discuss the trade-offs between different implementations of the HMBG. And in section 5 we showcase a few selected examples where the HMBG will have a major advantage over current approaches.

2. Multiplexed Bragg gratings

2.1. Bragg grating basics

Volume Bragg Gratings (VBG) are transmission gratings where the grating is written inside a piece of transparent material with as a periodic refractive index modulation. VBGs predominantly exhibit first-order diffraction while conventional transmission gratings diffract into multiple orders. These diffraction properties of Bragg gratings have been known since the 60's when Kogelnik proposed his coupled wave theory [12]. According to Kogelnik's theory a VBG optimally diffracts the wavelengths that satisfy the Bragg condition,

$$\lambda_B = 2n\Lambda \sin\theta_B. \tag{1}$$

λ_B is the Bragg wavelength, n the average refractive index of the material, Λ the pitch of the modulation and θ_B the angle of incidence. The Bragg wavelength is the wavelength that is matched to the period of the grating according to Eq. 1. The Bragg condition is nothing more than the blaze condition for conventional gratings. Wavelengths that deviate from the Bragg condition will be diffracted according to the grating equation,

$$\lambda = 2n\Lambda \left(\sin\theta_i + \sin\theta_d\right). \tag{2}$$

The geometry of the grating setup is similar to a normal grating spectrometer working in first order and can be seen in Fig. 2. The VBGs should not be confused with Fiber Bragg Gratings where the light travels along the modulation direction, which is the x-direction in Fig. 2.

The diffraction efficiency (DE) is the ratio between the amount of light that is diffracted into the first order and the amount of incoming light. A DE of 1 means that all the light is diffracted into the first order, while a DE of 0.5 means that half the light is diffracted and half the light remains in the zeroth order. Currently it is possible to manufacture VBGs with DEs above 99 percent [13]. The refractive index modulation that is necessary to obtain a 100 percent DE is [14],

$$\delta n = \frac{\lambda_B \cos\theta_B}{2t}. \tag{3}$$

Here δn is the amplitude of the refractive index modulation and t is the thickness of the grating. The differential optical-path delay that is accrued while travelling through the grating is $\delta\mathrm{OPD} = \delta n t/\cos\theta_B$. If Eq. 3 is used to substitute δn we arrive at $\delta\mathrm{OPD} = \lambda/2$. For optimal diffraction efficiency the δOPD has to be half a wave. When the δOPD differs from half-wave the DE lowers, which can happen either due to a wrong angle of incidence or a wavelength that deviates from the Bragg wavelength. If the thickness of the grating is increased it becomes easier to violate the phase matching conditions, and therefore a smaller wavelength range will be diffracted. This reduces the effective spectral bandwidth of the grating. The diffraction efficiency curves for different thicknesses are shown in Fig. 3, which shows that thicker gratings have a

Optics EXPRESS

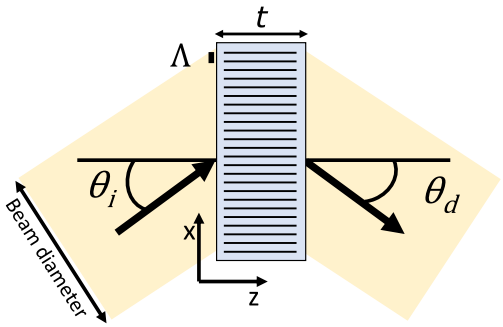

Fig. 2. The geometry of the Volume Bragg Grating setup where a collimated beam enters the grating from the left. The grating with a line spacing of Λ is modulated along the x direction. The incidence and diffracted angle are defined as θ_i and θ_d, respectively. The incident beam propagates from the left to the right through the grating. The thickness t is the width of the grating along the z-direction while the transverse size is the size along the x-direction.

sharper responses. We define the spectral bandwidth of the VBG as the half width at the first zero (HWFZ) [14],

$$\frac{\Delta\lambda}{\lambda_B} = \frac{\sqrt{3}}{4}\frac{\Lambda}{t}\frac{\cos\theta_B}{\sin^2\theta_B}. \tag{4}$$

Here $\Delta\lambda$ is the HWFZ of the diffracted spectrum. The current range of volume phase gratings make it possible to have a spectral bandwidth below 0.1 nm to more than 100 nm [14]. This spectral bandwidth should not be confused with the spectral resolving power of the grating. The spectral bandwidth is the spectral range that is diffracted, while the resolving power of a VBG follows the same equation as a normal grating and therefore depends on the number of lines N that are illuminated and the order of diffraction m. Hence the transverse size of the grating determines the resolving power, while the thickness determines the diffracted wavelength range.

2.2. Multiplexed Bragg gratings

It is possible to write multiple VBGs inside a single piece of glass where each one addresses a different Bragg wavelength allowing multiple spectral lines to be diffracted at once. By writing multiple VBGs the refractive index modulation is not a simple cosine or sine any more but a coherent superposition of many cosines. The multiplexed refractive index amplitude is,

$$\delta n(x) = \sum_{i}^{N} \delta n_i \cos\left(2\pi x/\,\Lambda_i\right). \tag{5}$$

Here $\delta n(x)$ is the total refractive index modulation, δn_i is the amplitude for each individual grating and Λ_i is the pitch of each grating. We propose to use a Highly Multiplexed Bragg Grating (HMBG) that multiplexes tens to hundreds of gratings, each grating addresses a spectral line of interest. Each spectral line will be chosen as the Bragg wavelength of its grating, and we adjust the pitch according to Eq. (1) in such a way that the diffracted output angle is the same. A lens can then re-image all the different beams onto a detector. Because all spectral lines are diffracted into the same output direction, they will end up at the same position on the detector. This optically combines all spectral lines. An example of the output of a HMBG can be seen in Fig. 4. Because all lines are optically combined we do not need to sample the full spectrum but only the footprint of a single spectral line.

Optics EXPRESS

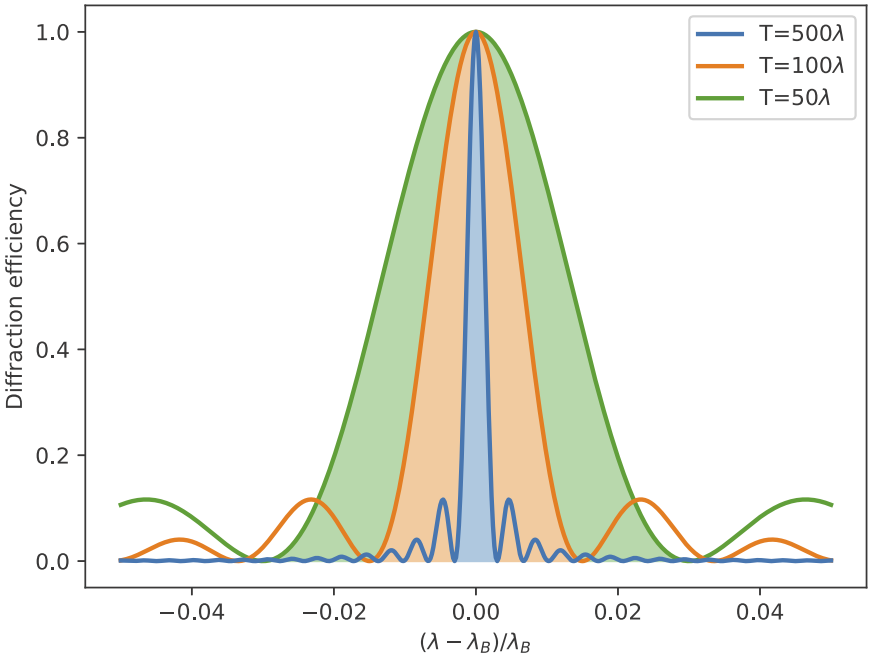

Fig. 3. The diffraction efficiencies as function of the relative deviation from the Bragg wavelength; each color represents a different grating thickness. The shaded region below the curves highlight the area that is spanned by the spectral bandwidth as defined by the Full Width at First Zero (FWFZ). To first order the diffraction efficiencies follow a sinc^2 profile.

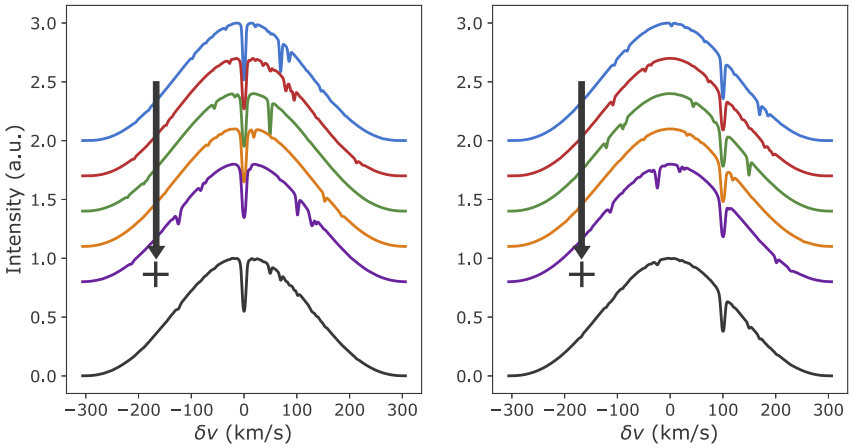

Fig. 4. Two example signals from the HMBG for 5 randomly chosen lines from a stellar spectrum. The individual responses for each grating are shown by the coloured spectra. For readability each spectrum was offsetted in the vertical direction. The HMBG creates a slice around each spectral line of interest onto the detector. The actual detected response is the integrated signal shown in black. The envelop of the signal is the diffraction efficiency curve, and if the species of interest is present we can see the average line profile at the objects Doppler shift. Depending on the velocity of the target the average line profile will coherently shift and remains detectable as can be seen in the figure on the right where the object has a Doppler shift of 100 km/s. All spectral features other than the spectral lines of interest are washed out due to the incoherent sum of different slices.

Optics EXPRESS

If we now assume that the spectral bandwidth of the grating is broader than the spectral lines of interest, then the spectrum of the object will be diffracted by the VBG such that a narrow slice around the line of interest will be isolated. The multiplexed grating will then create an incoherent sum of the individual slices, where the center of the summed spectra will show the average line profile. When many lines are multiplexed it becomes problematic to describe the dispersion axis with a wavelength coordinate as there are many wavelengths superimposed on the same pixel. The output angle of the relative change of wavelength can be found with the grating equation,

$$\frac{\delta\lambda}{\lambda_B} = \frac{1}{2}\frac{\sin(\theta_B + \Delta\theta) - \sin\theta_B}{\sin\theta_B}. \tag{6}$$

With $\delta\lambda$ the deviation from the Bragg wavelength. From this relation we can see that each output angle corresponds to the same amount of relative wavelength shift irrespective of the chosen λ_B. Under the assumption that the spectral lines of interest are chosen as the λ_B for their respective grating, they will all propagate in the same direction. We can relate the relative change of the wavelength to the relative radial velocity of the object of interest. Substituting the formula the for classical Doppler shifts we obtain,

$$\frac{\delta v}{c} = \frac{1}{2}\frac{\sin(\theta_B + \Delta\theta) - \sin\theta_B}{\sin\theta_B}. \tag{7}$$

The output angle is independent of any of the grating periods and only depends on the velocity shift $\frac{\delta v}{c}$. The HMBG maps the quasi-matched filter response of a species at a certain radial velocity to an output angle independent of the chosen grating period; it is therefore natural to use velocity coordinates.

The velocity shift that can be resolved depends on the spectral resolving power of the grating, $\delta v = c/R$. The velocity bandwidth is set by the spectral bandwidth, which in turn is set by the thickness of the grating. A thicker grating will have a narrower velocity bandwidth, which can be derived from Eq. (6),

$$\frac{\Delta v}{c} = \frac{\sqrt{3}}{4}\frac{\Lambda}{t}\frac{\cos\theta_B}{\sin^2\theta_B}. \tag{8}$$

Here Δv is the velocity bandwidth. These two parameters need to be taken into account during the design of a HMBG. The design of a HMBG starts with the choice of a velocity bandwidth, because this determines the minimum spacing between spectral lines that can be multiplexed together. Then the spectral lines can be chosen and the grating period can be calculated from Eq. 1.

2.3. Simulating diffraction efficiencies

To design an efficient instrument the grating diffraction efficiency should not decrease with the number of lines that are multiplexed, otherwise there would be no point in trying to add more lines. Multiplexed Bragg gratings are usually calculated with Rigorous Coupled Wave Theory [15]. This is an extension of the simple coupled-wave theory of Kogelnik. The downside to RCWT-like codes is that they couple all the modes that are present in the system. The gratings will couple with each other, and if we want to know the diffraction efficiencies of M diffraction orders on N multiplexed spectra, we need to include M^N modes. For $M = 2$, which includes the 0th and 1st order, and $N = 100$ this already leads to an unmanageable computing time.

The RCWT only needs to be used if the spectral lines are close to each other. As said before if the lines are separated enough, the response can be calculated as an incoherent superposition of the individual responses. To check this we wrote a symmetric split-step Fourier beam propagation code (BPM) [16]. This code can propagate an electric field through arbitrary refractive index profiles. The speed of the code only depends on the spatial sampling of the grating, and therefore

Optics EXPRESS

it is independent of the amount of multiplexed gratings as opposed to RCWT-like codes. The BPM code has been validated on several test cases including free-space propagation, waveguide propagation and diffraction from a single Volume Bragg Grating. In all cases the power was conserved to better than 0.1 %, and the single VBG simulation showed a diffraction efficiency curve that followed the curve as derived by Kogelnik.

As an initial test case, we created N randomly positioned spectral lines between 0.5 μm to 1.0 μm. The lines are separated by at least three times the FWHM of the spectral bandwidth [17]. This directly gives the spectral bandwidth necessary for the uncoupled regime. The peak diffraction efficiency of each grating is then calculated by propagating its Bragg wavelength. The average diffraction efficiency of the grating converges to 100 percent for all number of lines that we tried. The grating that multiplexes a 100 lines converges to 97 percent, which is slightly lower than 100 percent because of numerical inaccuracies. The BPM code includes all possible types of crosstalk between the gratings, and we see no major cross talk, which we expected based on [17]. This result encouraged us to use a simpler model where the response is just a superposition of the individual responses.

3. Advantages of multiplexed Bragg gratings

Our method has several advantages over recording the full spectrum. The most important one is that it can reduce the amount of pixels per spatial pixel (spaxel) considerably because we do not need to record the complete spectrum. This substantially decreases the required number of pixels per spatial pixel and makes it possible to increase the field of view compared to a conventional spectrograph for a fixed detector size. The downside to this method is that we lose the full spectral information. The number of pixels required per spaxel depends on the velocity bandwidth and velocity resolution. The bandwidth is given by the maximum Doppler shift one wants to measure. The velocity resolution is directly related to an equivalent spectrograph resolution,

$$\delta v = \frac{c}{N_{\text{sampling}} R}. \tag{9}$$

Here δv is the velocity sampling, and N_{sampling} is the number of pixels per spectral resolving element and R is the resolving power defined as $R = \lambda/\delta\lambda$. The amount of pixels that is necessary to sample the full velocity bandwidth on a detector is,

$$N_{\text{v}} = \frac{\Delta v}{\delta v} = \frac{\Delta v}{c} N_{\text{sampling}} R. \tag{10}$$

To know the reduction in detector space we need to compare this to a traditional spectrograph. A spectrograph must have a bandwidth $\Delta\lambda$ that is large enough to contain all the spectral lines. The wavelength sampling should be,

$$\delta\lambda = \frac{\lambda}{N_{\text{sampling}} R}. \tag{11}$$

The amount of pixels this will require is

$$N_{\lambda} = \frac{\Delta\lambda}{\delta\lambda} = \frac{\Delta\lambda}{\lambda} N_{\text{sampling}} R. \tag{12}$$

The reduction in detector space is then

$$N_{\text{gain}} = \frac{N_{\lambda}}{N_{\text{v}}} = \frac{c}{\Delta v} \frac{\Delta\lambda}{\lambda}. \tag{13}$$

Interestingly the detector space reduction is independent of the resolving power and purely depends on the bandwidths that are required. Following this equation we estimate the amount of

Optics EXPRESS

detector space that can be gained for Earth observations. Earth observations are usually done from Low-Earth Orbit (LEO) satellites that have velocities of roughly 10 km/s. We should therefore select a velocity range that can easily accommodate this speed, which we chose at $\Delta v = \pm$ 50 km/s. To contain the most interesting lines we would like spectral coverage from 1μm to 3.5 μm. For this spectral range and velocity bandwidth we estimate that the detector area reduction is between 2500 and 18000, depending on which wavelength is Nyquist sampled.

The signal-to-noise(SNR) ratio of the HMBG signal is, to first order,

$$\mathrm{SNR} = \frac{F_0\sqrt{NR}}{\sqrt{F_0 + \sigma_\mathrm{D}^2}}. \tag{14}$$

Here F_0 is the average photon flux ratio between the continuum and the selected spectral lines, N the number of spectral lines that are multiplexed, R the spectral resolving power and σ_D the read and dark noise. Comparing this to the SNR ratio of normal spectroscopy,

$$\mathrm{SNR} = \frac{F_0\sqrt{NR}}{\sqrt{F_0 + \sigma_\mathrm{D}^2 N}}, \tag{15}$$

we see that the effects of read noise and dark noise are decreased by the number of spectral lines that are multiplexed because the spectral lines are added together on the same pixel. For faint signals the HMBG will achieve higher SNR compared to normal spectroscopy because the HMBG spreads the light over fewer pixels. A disadvantage of the HMBG is that it cannot multiplex all spectral lines, as some will be too close together. Therefore the HMBG cannot use all available spectral lines, and the SNR of the HMBG compared to normal spectroscopy will be lower in the photon-noise limited regime. To estimate the SNR decrease we used the spectra of Fig. 1 to estimate the number of lines and the average line depth for each species. We again assumed a velocity bandwidth of $\Delta v = \pm$ 50 km/s, and found that we are able to multiplex on average 75 spectral lines per species from 1.6 μm to 1.8 μm. Not all spectral lines are of the same importance as their depth, and therefore their contribution to the SNR budget, varies. The ratios of the SNR of the HMBG compared to the SNR of normal spectroscopy for the three species are, 0.5 for CO_2, 0.77 for H_2O and 0.77 for CH_4. The HMBG will be at most a factor of 2 less sensitive in the photon-noise limited regime for the considered case.

Another advantage of the multiplexed grating over gas-cell correlations is that it is also allows for correlation measurements for species that are difficult to contain in a gas cell. Therefore the HMBG can achieve the same kind of sensitivity as the gas-cell correlators but for a wider range of objects. The second advantage compared to the gas-cell sensor is that the HMBG measurements retain spectral line information.

4. Multiplexed Bragg grating implementation

4.1. Static system

There are several ways to implement multiplexed gratings. The simplest solution is to physically put several transmission gratings in series [18]. The disadvantage of stacking gratings is that it quickly becomes a very thick optical element as the number of multiplexed lines increase. For a few tens of lines the thickness can quickly reach several tens of centimeters, which will require a substantial over-sizing of the grating to avoid issues with vignetting. The different gratings will also diffract the light at different planes as the gratings are physically stacked after each other. This will put very stringent requirements on the imaging lens, if at all possible, to make sure that all the chosen spectral lines will still fall on the same location on the detector. Therefore, if a multiplexed grating with many lines is required, it will be necessary to write the gratings in a

Optics EXPRESS

single piece of glass. There are several manufacturing techniques that can write complicated refractive-index profiles. For Volume Bragg Gratings the most common technique is holography.

In holographic writing two beams are tilted with respect to each other, which creates a sinusoidal interference pattern. The angle between the beams can be adjusted to create the correct line spacing. With holography the different gratings will be written sequentially. This creates an incoherent addition of the gratings in the material, leading to a refractive index profile given by,

$$\delta n(x) = \sum_{i}^{N} \delta n_i \frac{1 + \cos\left(2\pi x / \Lambda_i\right)}{2}. \tag{16}$$

Due to the incoherent addition the refractive index modulation grows linearly with the number of spectral lines, quickly saturating the writing material [19,20]. This can be circumvented by coherently writing the gratings that create a refractive index profile as determined by Eq. (5). For a coherent multiplexed grating the refractive index modulation grows as the square root of the number of gratings allowing for many more gratings to be written in the material. Recent literature on the dynamic range of holographic materials shows that the maximum refractive index modulation can be as high as 0.03 [21]. A grating with a thickness of 1000 waves at a 25 degree incidence angle requires an index modulation of 0.00045 according to Eq. (3). The number of lines that can be written before the material saturates is about 60 for incoherent writing while coherent writing could reach roughly 4000 lines. This demonstrates the clear advantage of the coherent approach over the incoherent approach, but it requires a different manufacturing strategy.

Direct write methods where the refractive index is modified point-by-point can write coherent multiplexed gratings. An example of a highly multiplexed grating is the OH suppression filter written inside single-mode fibers [11,22]. This filter is able to multiplex tens to hundreds of gratings for the suppression of the atmospheric OH lines. Direct write techniques are now also being used to write 2D gratings that can achieve diffraction efficiencies higher than 90% [23–25].

4.2. Dynamic system

The down-side of writing a multiplexed grating into glass is that the grating cannot be changed afterwards. The resulting HMBG can only measure the signal of a single species. This leads to a cumbersome system for situations where multiple species need to be measured. An active system where the spectral template can be changed on the fly would address this issues; it can be achieved with acousto-optical (AO) gratings. In acousto-optical materials the local refractive index can be changed by passing sound waves through the transparent material. High-quality acousto-optical materials have been on the rise in the past decades and have become quite common in recent years. Low-resolution versions of the proposed idea have been in use as acousto-optical tunable filters. In AOTFs the sound waves are tuned to the central wavelength to create bandpass filters that are digitally tunable. There are versions which can have multiple bandpasses at the same time. Another advantage of the AOTFs is the use of multiple transducers to create the sound waves. If the transducers are used as a phased array one can create an arbitrary 3D refractive index profile [26]. This can be used to apodize the sidelobes of the diffraction efficiency curve for a more uniform efficiency over the spectral bandwidth because for normal VBGs the efficiency drops off as the spectral lines of interest are more Doppler shifted.

4.3. Challenges when implementing as a hyper-spectral imager

An sketch of the proposed hyperspectral camera can be seen in Fig. 6. The main challenge for the HMBG for large fields of view will be the acceptance angle of the grating itself. The output angle of the grating shifts if the input angle is different from the Bragg angle. If the angular shift is too large, the spectral line of interest can move beyond the spectral bandwidth and make it

Optics EXPRESS

unobservable. This constraints the acceptance angle of the HMBG. The output angle can be found with the grating equation,

$$\lambda = n\Lambda \left(\sin\left[\theta_B + \theta_{\text{in}}\right] + \sin\left[\theta_B + \theta_{\text{out}}\right]\right). \tag{17}$$

Here θ_{in} and θ_{out} are the deviations from the Bragg angle. Expanding the input and output angles around the Bragg angle and subtracting the Bragg wavelength leads to,

$$\lambda - \lambda_B = n\Lambda \cos\theta_B \left(\theta_{\text{in}} + \theta_{\text{out}}\right). \tag{18}$$

From this equation we can see that when we consider the Bragg wavelength ($\lambda - \lambda_B = 0$), the output angle will shift by the same amount as the input angle is shifted away from the Bragg angle. The input acceptance angle is therefore the same as the output acceptance angle. We can derive the maximum output angle from Eq. (7) using the velocity bandwidth. The acceptance angle as a function of velocity bandwidth is shown in Fig. 5 for several different Bragg angles. Here we can see that the angle of acceptance is smaller than one degree for most cases.

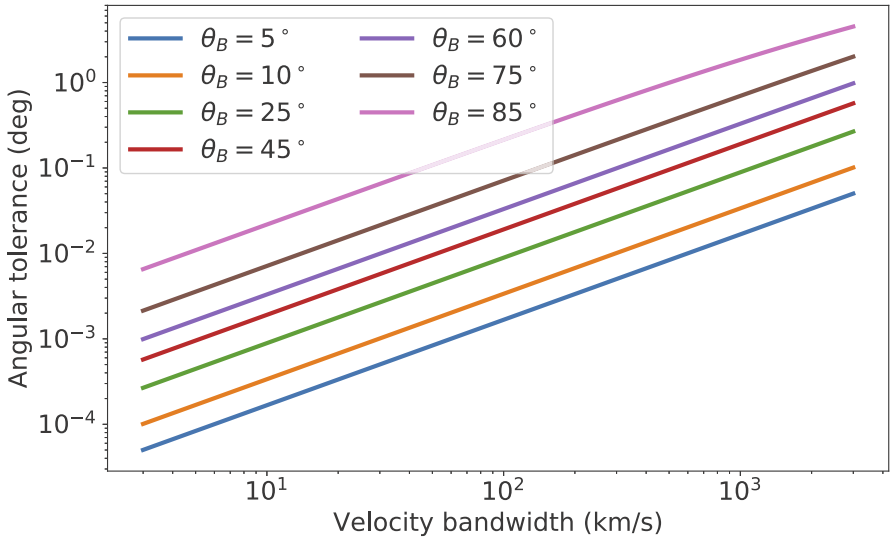

Fig. 5. The angular tolerance as a function of velocity bandwidth. The velocity bandwidth is shown from 3 to 3000 km/s. The colored lines represent different Bragg angles. As the Bragg angle increases, the acceptance angle increases.

Due to the small acceptance angle of the HMBG any deviation of the input angle from the Bragg angle needs to be minimized. Therefore the HMBG can only accept slit-like inputs where all light has the same angle of incidence on the grating. For two-dimensional field-of-views we need to map the field into a slit, which can be done with either advanced image slicers [27] or fiber bundles [28].

Optics EXPRESS

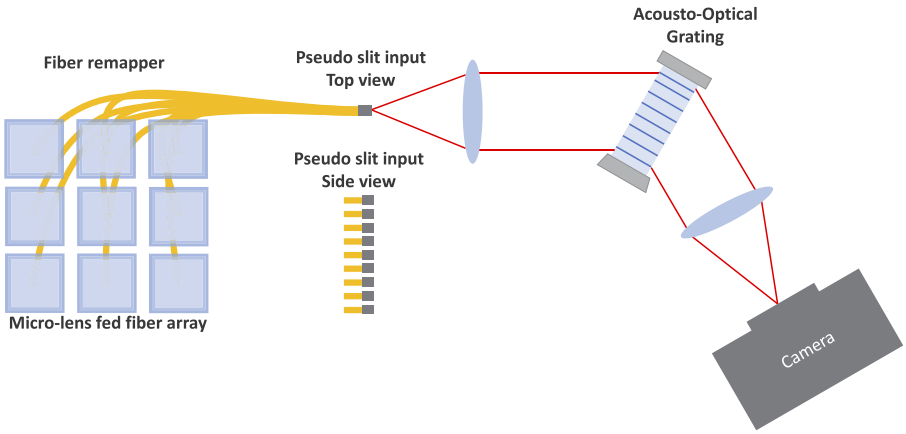

Fig. 6. A sketch of the proposed setup. The two-dimensional input is remapped through a fiber array into a pseudo-slit. The pseudo-slit feeds the spectrograph in a first-order grating configuration.

5. Applications of the highly multiplexed Bragg grating

5.1. Highly multiplexed Bragg Grating instrument model

The HMBG response is simulated with a simple model where all gratings are considered independently. This assumption is valid as long as we make sure that all gratings are in the uncoupled regime. For this model the intensity on a pixel for grating i with a fixed input angle θ_{in} is,

$$I_i(\theta) = \int S(\lambda)\,\eta_i(\lambda, \theta_{\text{in}}) H_i(\lambda, \theta, \theta_{\text{in}})\,d\lambda, \tag{19}$$

where θ is the output angle of the grating, S is the input spectrum of the scene, η_i is the diffraction efficiency of the grating and H_i is the line spread function (LSF). The LSF is taken as a simple sinc function with a full-width half maximum that is matched to the spectral resolving power R. This shape of the LSF arises because of the assumption of an uniformly illuminated square grating. The spectral dispersion of the LSF is calculated from the grating equation. For a multiplexed grating we sum over all gratings i, which results in the detector signal,

$$I(\theta) = \sum_i I_i(\theta). \tag{20}$$

5.2. Abundance retrieval of molecular species

A key aspect of remotely sensing a gas is to measure the amount of gas that is present, which can be achieved with the HMBG. Here we first show that for optically thin lines there exists a linear relation between the amount of gas and the HMBG output. We start by considering a single, plane-parallel layer of material for which the transmission can be written as,

$$T(\lambda) = e^{-\tau(\lambda)}. \tag{21}$$

Here $T(\lambda)$ is the transmission as a function of wavelength λ, and τ is the total optical depth at wavelength λ. From here on the explicit dependence of T and τ on λ will be left out. For a

Optics EXPRESS

mixture of gases the optical depth can be described by,

$$\tau = \sum_i \tau_i = \sum_i n_i \sigma_i. \tag{22}$$

This sum is over all species i with a column density n_i and absorption cross-section σ_i. The optical depth of each individual species is the product of the wavelength-independent column density and the absorption cross-section. In the optically thin regime $\tau \ll 1$ the transmission becomes,

$$T = 1 - \tau + O(\tau^2) \approx 1 - \sum_i n_i \sigma_i. \tag{23}$$

For optically thin lines the transmission depends linearly on the column density. Our model of the HMBG, according to Eq. (19), is a linear transformation from the input spectrum to the multiplexed dispersed measurement. Therefore there should be a linear relation between the HMBG output and the column density for optically thin lines.

This relation can be empirically calibrated by measuring the response of the HMBG to known amounts of each species of interest. The individual measurements from templates are stacked together in one vector $\vec{S}$. These measurements are then fitted by the following linear model,

$$\vec{S} = A\vec{n} + \vec{b}. \tag{24}$$

Here $\vec{S}$ is the stacked response, which contains the full line shape information, for all templates, A is the transformation matrix and $\vec{b}$ is the offset. We test the accuracy of the retrieval with a mixture of H_2O, CH_4 and CO_2. The HMBG template is made from the spectral lines shown in Fig. 1. For each template we search for the strongest spectral lines in the wavelength range. Our algorithm searches iteratively for the strongest spectral line and adds it to the line-list. Each time a line is selected we check if the distance to any of the spectral lines in our line-list is smaller than a threshold. If it is smaller we reject the new line and go to the next strongest line. The threshold is set at three times the FWHM of the spectral bandwidth to make sure we are in the regime where the gratings are uncoupled [17]. This is not necessarily the optimal way of choosing which lines to multiplex for the different templates, but one that is relatively easy to implement.

We used column densities from $n = 10^{10} - 10^{15}$ cm^{-2} to determine the linear retrieval model parameters since the simulations had shown that these densities were well within the optically thin regime. Then we applied this model to retrieve densities from $n = 10^{10} - 10^{21}$ cm^{-2}. The results are shown in Fig. 7. The column density of each species is retrieved over the full range. Methane shows a small deviation above 10^{19}cm^{-2} where the selected spectral lines become optically thick. The linear response can be extended over a larger range by selecting only spectral lines that are optically thin for the column densities of interest, which is an advantage of dynamically selecting the spectral template. This is not possible with gas-cell correlators because the gas-cell contains all spectral lines including the lines that become optically thick. There is also cross-talk between the species. The cross-talk of methane to the other species is the strongest, which was expected as the cross-section of methane is the largest in this range. The cross-talk itself grows as the square of the column density because of the linear approximation of Eq. (23). The cross-talk can be decreased by carefully selecting the spectral lines that will not blend with the lines of other species. This can be accomplished by orthogonalizing the cross-section spectra of the different species with a Gram-Schmidt procedure [29]. The influence of cross-talk can also be reduced by selecting a larger or different wavelength range that includes more distinct lines.

5.3. Molecule maps

To estimate the accuracy of the linear extraction for a mixture of gases we simulated a single two-dimensional map with a variable mixture of H_2O, CH_4 and CO_2. The spatial distributions

Optics EXPRESS

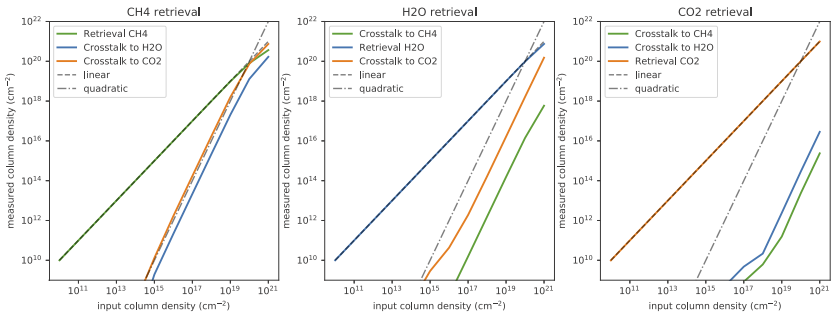

Fig. 7. This figures shows the accuracy of the HMBG in combination with the linear retrieval algorithm for estimating the column density for single species. The input column density versus the retrieved column density is shown for CH_4, H_2O and CO_2. While each species has its own measurement template in the HMBG, there will still be cross-talk in due to non-linearities that are not taken into account in the retrieval. The cross-talk lines show the influence that the presence of the other species have on the retrieval. In the optically thin regime the cross-talk is very small and grows as the square of the column density.

of the gases were randomly created with column densities ranging from 10^{10}cm^{-2} to 10^{18}cm^{-2}. For every pixel we simulated the response to the different templates from the previous section and applied the linear reconstructor to measure the column densities. The results can be seen in Fig. 8. The method recovers the column densities with high accuracy and precision. The average relative reconstruction error is much smaller than one percent. We can see that in the regions with a higher density of CH_4 there is more cross-talk. This influences the reconstruction of the other species. The non-linear cross-talk is stronger for CO_2 than for H_2O, which was also expected based on Fig. 7.

5.4. *Exoplanet detection*

Another application of the HMBG technique is in the field of astronomy for the detection and/or characterization of exoplanet atmospheres. The main problem for exoplanet detection is the contrast in intensity between the host star and the planet itself. The host star is usually brighter by a factor of a million for the largest and hottest exoplanets to a billion for old and cold Earth-like planets [30]. The standard method for detecting exoplanets is through very careful subtraction of the Point-Spread Function (PSF) of the star [30,31]. If the incoming wavefront changes the PSF of the star, then this subtraction scheme will not reach the ultimate sensitivity given by photon noise. This can happen for example due to turbulence in the Earth's atmosphere or slowly varying instrumental wavefront errors [32].

High-resolution spectroscopy ($R \approx 100000$) has been proposed as a solution to find planets because we can discern the difference between the star and the planet based on the difference in their spectral lines [29,33]. The downside of the method is its need for a large amount of pixels, and therefore it has a small discovery space. With the HMBG we can do exactly the same measurement but with less pixels, which substantially increases the discovery space for exoplanets. To show the potential of the HMBG we simulated a dataset of a star with a planet around it. The simulation has been done with wavefront errors that vary in time to simulate residual turbulence and varying instrumental effects. We used a PHOENIX model [34] with an effective temperature of 6000 K to create a sun-like spectrum for the star. For the planet spectrum we assumed that we only see reflected starlight and took the spectrum as a Doppler-shifted and flux-scaled replica of the stellar spectrum with a contrast of 10^{-6}. To search for the planet we created a HMBG template that stacked the 120 deepest lines of the stellar spectrum in the wavelength range from 0.9μm to 1.1μm. The velocity bandwidth around each line is 100 km/s,

Optics EXPRESS

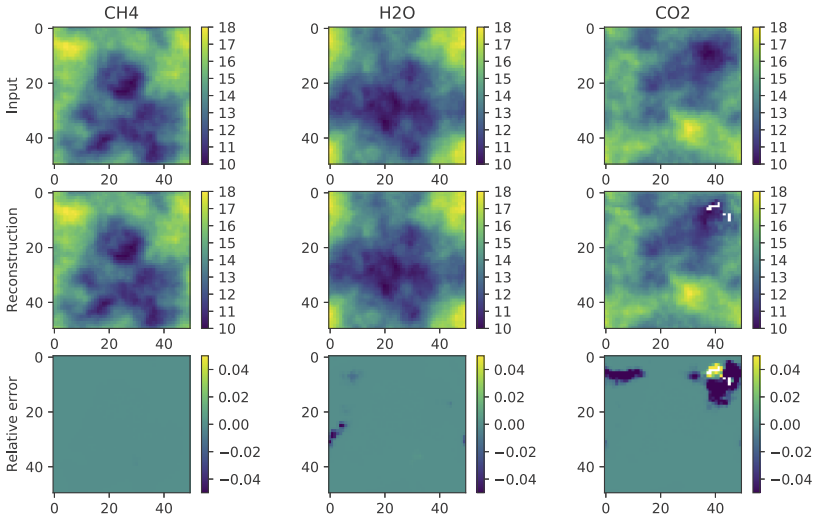

Fig. 8. The retrieval of the column density is shown separately for CH_4, H_2O and CO_2. The top row shows the input column density and the middle row shows the retrieved column density. The bottom row shows the relative error in the retrieval. The relative error for CH_4 is much smaller than a percent. The other two species have larger relative errors with a maximum relative error of 15 percent. The large deviations occur at the places with high CH_4 column densities where the non-linearities that were not taken into account in the retrieval become important.

and the resolving power is set to 3 km/s. We expect to see two absorption lines in the multiplexed signal, one from the star at zero velocity and one at 25 km/s, which is the planet's radial velocity.

The planet signal can be recovered from the HMBG data cube by subtracting the spatially averaged HMBG measurement from every point in the field of view. The results of the simulations can be seen in Fig. 9 where we compare the HMBG planet detection with a classical PSF subtraction algorithm, namely Angular Differential Imaging (ADI) [31]. ADI creates a references PSF by averaging the PSF in time while the field is rotating. Due to the field rotation the apparent position of the planet will rotate and, if the planet rotates enough, it will not appear in the time-averaged PSF. The limits of ADI will be mainly dictated by how fast the PSF changes due to varying wavefront errors and how fast these will average out. In our simulations the ADI technique is limited to a contrast of 3000 at an angular distance of 5 λ/D for this dataset, while the HMBG can still clearly detect the planet at a contrast of 10^{-6}. This simple simulation shows that the HMBG measurements are robust to the speckle noise, while algorithms like ADI are not. The HMBG can therefore image fainter objects at smaller angular separations where observations are strongly speckle-noise limited.

Optics EXPRESS

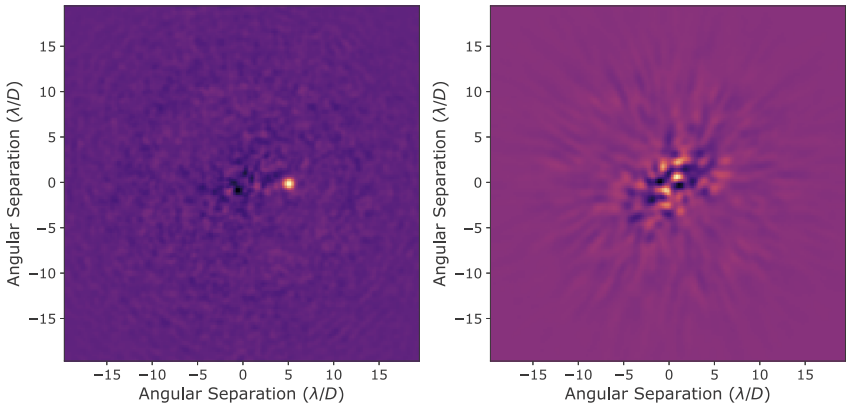

Fig. 9. The HMBG holds great promise for the detection and characterization of exoplanets. The two figures show the greatly enhanced capabilities of the HMBG (left) vs the classical approach currently used by astronomers (right). The planet is clearly visible with the HMBG while the ADI processed data still show strong speckle noise. This demonstrates that the HMBG is not limited by speckle noise, which is the major limiting factor for current observations of exoplanets.

6. Conclusion

We have shown that Volume Bragg gratings with many multiplexed gratings can be used for the quantitative detection of gas species with a significantly smaller detector than a comparable hyperspectral imager. This allows for a larger field-of-view given the same amount of detector real estate. We proposed to implement the HMBG with acousto-optical gratings that can be dynamically tuned at high speed and work from the near UV to the infrared. The dynamical aspect of the acousto-optical materials will allow us to use the same optics to detect different species. This simplifies the whole instrument as we can digitally choose what we would like to observe and thereby make the instrument highly flexible.

A major advantage of the HMBG over the traditional gas-cell correlation is that the HMBG retains the line profile and information about the continuum. This enables us to estimate column densities over a large range of densities and species mixtures. And we have also shown its use as a method for detecting reflected light from exoplanets, but detailed end-to-end simulations will be necessary to determine the exact performance gain of the HMBG compared to traditional exoplanet detection methods. The next step will be to build a prototype HMBG to verify the proposed concept and explore several aspects of the acousto-optical implementation such as the limits of the multiplexing capability and the angular tolerance.

Funding

Nederlandse Organisatie voor Wetenschappelijk Onderzoek (VICI 639.043.107); Fundação de Amparo à Pesquisa do Estado de São Paulo.

References

1. F. Snik, J. H. H. Rietjens, A. Apituley, H. Volten, B. Mijling, A. D. Noia, S. Heikamp, R. C. Heinsbroek, O. P. Hasekamp, J. M. Smit, J. Vonk, D. M. Stam, G. Harten, J. Boer, and C. U. Keller, 3187 iSPEX citizen scientists, "Mapping atmospheric aerosols with a citizen science network of smartphone spectropolarimeters," Geophys. Res. Lett. **41**(20), 7351–7358 (2014).
2. D. J. Williams, B. L. Feldman, T. J. Williams, D. Pilant, P. G. Lucey, and L. D. Worthy, "Detection and identification of toxic air pollutants using airborne LWIR hyperspectral imaging," in *Multispectral and Hyperspectral Remote*

Optics EXPRESS

Sensing Instruments and Applications II, vol. 5655 of *Proc. SPIE* A. M. Larar, M. Suzuki, and Q. Tong, eds. (2005), pp. 134–141.

3. K. Wu, Y. Feng, G. Yu, L. Liu, J. Li, Y. Xiong, and F. Li, "Development of an imaging gas correlation spectrometry based mid-infrared camera for two-dimensional mapping of co in vehicle exhausts," Opt. Express **26**(7), 8239–8251 (2018).
4. R. V. Kochanov, I. Gordon, L. Rothman, P. Wcisło, C. Hill, and J. Wilzewski, "Hitran application programming interface (hapi): A comprehensive approach to working with spectroscopic data," J. Quant. Spectrosc. Radiat. Transfer **177**, 15–30 (2016).
5. L. S. Rothman, I. E. Gordon, Y. Babikov, A. Barbe, D. Chris Benner, P. F. Bernath, M. Birk, L. Bizzocchi, V. Boudon, L. R. Brown, A. Campargue, K. Chance, E. A. Cohen, L. H. Coudert, V. M. Devi, B. J. Drouin, A. Fayt, J. M. Flaud, R. R. Gamache, J. J. Harrison, J. M. Hartmann, C. Hill, J. T. Hodges, D. Jacquemart, A. Jolly, J. Lamouroux, R. J. Le Roy, G. Li, D. A. Long, O. M. Lyulin, C. J. Mackie, S. T. Massie, S. Mikhailenko, H. S. P. Muller, O. V. Naumenko, A. V. Nikitin, J. Orphal, V. Perevalov, A. Perrin, E. R. Polovtseva, C. Richard, M. A. H. Smith, E. Starikova, K. Sung, S. Tashkun, J. Tennyson, G. C. Toon, V. G. Tyuterev, and G. Wagner, , "The hitran2012 molecular spectroscopic database," J. Quant. Spectrosc. Radiat. Transfer **130**, 4–50 (2013).
6. D. G. Manolakis, "Overview of algorithms for hyperspectral target detection: theory and practice," in *Society of Photo-Optical Instrumentation Engineers (SPIE) Conference Series*, vol. 4725 (2002), pp. 4725–47214.
7. M. Brogi, I. A. Snellen, R. J. de Kok, S. Albrecht, J. Birkby, and E. J. de Mooij, "The signature of orbital motion from the dayside of the planet τ boötis b," Nature **486**(7404), 502–504 (2012).
8. Q. M. Konopacky, T. S. Barman, B. A. Macintosh, and C. Marois, "Detection of carbon monoxide and water absorption lines in an exoplanet atmosphere," Science **339**(6126), 1398–1401 (2013).
9. B. Macintosh, J. R. Graham, T. Barman, R. J. De Rosa, Q. Konopacky, M. S. Marley, C. Marois, E. L. Nielsen, L. Pueyo, A. Rajan, J. Rameau, D. Saumon, J. J. Wang, J. Patience, M. Ammons, P. Arriaga, E. Artigau, S. Beckwith, J. Brewster, S. Bruzzone, J. Bulger, B. Burningham, A. S. Burrows, C. Chen, E. Chiang, J. K. Chilcote, R. I. Dawson, R. Dong, R. Doyon, Z. H. Draper, G. Duchêne, T. M. Esposito, D. Fabrycky, M. P. Fitzgerald, K. B. Follette, J. J. Fortney, B. Gerard, S. Goodsell, A. Z. Greenbaum, P. Hibon, S. Hinkley, T. H. Cotten, L. W. Hung, P. Ingraham, M. Johnson-Groh, P. Kalas, D. Lafreniere, J. E. Larkin, J. Lee, M. Line, D. Long, J. Maire, F. Marchis, B. C. Matthews, C. E. Max, S. Metchev, M. A. Millar-Blanchaer, T. Mittal, C. V. Morley, K. M. Morzinski, R. Murray-Clay, R. Oppenheimer, D. W. Palmer, R. Patel, M. D. Perrin, L. A. Poyneer, R. R. Rafikov, F. T. Rantakyrö, E. L. Rice, P. Rojo, A. R. Rudy, J. B. Ruffio, M. T. Ruiz, N. Sadakuni, L. Saddlemyer, M. Salama, D. Savransky, A. C. Schneider, A. Sivaramakrishnan, I. Song, R. Soummer, S. Thomas, G. Vasisht, J. K. Wallace, K. Ward-Duong, S. J. Wiktorowicz, S. G. Wolff, and B. Zuckerman,, "Discovery and spectroscopy of the young jovian planet 51 eri b with the gemini planet imager," Science **350**(6256), 64–67 (2015).
10. A. Verlaan, W. Klop, H. Visser, H. van Brug, and J. Human, "Higs-instrument: design and demonstration of a high performance gas concentration imager," in *International Conference on Space Optics-ICSO 2016*, vol. 10562 (International Society for Optics and Photonics, 2017), p. 105625Z.
11. J. Bland-Hawthorn, M. Englund, and G. Edvell, "New approach to atmospheric OH suppression using an aperiodic fibre bragg grating," Opt. Express **12**(24), 5902–5909 (2004).
12. H. Kogelnik, "Coupled wave theory for thick hologram gratings," Bell Syst. Tech. J. **48**(9), 2909–2947 (1969).
13. A. L. Glebov, O. Mokhun, A. Rapaport, S. Vergnole, V. Smirnov, and L. B. Glebov, "Volume Bragg gratings as ultra-narrow and multiband optical filters," in *Micro-Optics 2012*, vol. 8428 of *Proc. SPIE* (2012), p. 84280C.
14. I. V. Ciapurin, L. B. Glebov, and V. I. Smirnov, "Modeling of Gaussian beam diffraction on volume Bragg gratings in PTR glass," in *Practical Holography XIX: Materials and Applications*, vol. 5742 of *Proc. SPIE* T. H. Jeong and H. I. Bjelkhagen, eds. (2005) pp. 183–194.
15. M. Moharam and T. Gaylord, "Rigorous coupled-wave analysis of planar-grating diffraction," J. Opt. Soc. Am. **71**(7), 811–818 (1981).
16. S. Blanes and P. Moan, "Splitting methods for the time-dependent schrödinger equation," Phys. Lett. A **265**(1-2), 35–42 (2000).
17. X. Fu, M. Fay, and J. M. Xu, "1×8 supergrating wavelength-division demultiplexer in a silica planar waveguide," Opt. Lett. **22**(21), 1627–1629 (1997).
18. Z. Alessio, L. Marco, R. Marco, and B. Andrea, "Spectral multiplexing using stacked VPHGs - Part I," ArXiv e-prints (2017).
19. J. H. Hong, P. Yeh, D. Psaltis, and D. Brady, "Diffraction efficiency of strong volume holograms," Opt. Lett. **15**(6), 344–346 (1990).
20. S. Kaim, S. Mokhov, I. Divliansky, V. Smirnov, J. Lumeau, B. Y. Zeldovich, and L. B. Glebov, "Saturation of multiplexed volume bragg grating recording," J. Opt. Soc. Am. A **32**(1), 22–27 (2015).
21. M. D. Alim, S. Mavila, D. J. Glugla, C. Wang, P. D. Nystrom, A. C. Sullivan, C. N. Bowman, and R. R. McLeod, "High dynamic range two-stage photopolymer materials through enhanced solubility high refractive index writing monomers," in *Society of Photo-Optical Instrumentation Engineers (SPIE) Conference Series*, vol. 10558 (2018), p. 105580D
22. S. C. Ellis, J. Bland-Hawthorn, J. Lawrence, A. J. Horton, C. Trinh, S. G. Leon-Saval, K. Shortridge, J. Bryant, S. Case, M. Colless, W. Couch, K. Freeman, L. Gers, K. Glazebrook, R. Haynes, S. Lee, H.-G. Löhmannsröben, J.

Optics EXPRESS

O'Byrne, S. Miziarski, M. Roth, B. Schmidt, C. G. Tinney, and J. Zheng, "Suppression of the near-infrared OH night-sky lines with fibre Bragg gratings - first results," Mon. Not. R. Astron. Soc. **425**(3), 1682–1695 (2012).
23. M. Mikutis, T. Kudrius, G. Šlekys, D. Paipulas, and S. Juodkazis, "High 90% efficiency bragg gratings formed in fused silica by femtosecond gauss-bessel laser beams," Opt. Mater. Express **3**(11), 1862–1871 (2013).
24. D. G. MacLachlan, R. R. Thomson, C. R. Cunningham, and D. Lee, "Mid-infrared volume phase gratings manufactured using ultrafast laser inscription," Opt. Mater. Express **3**(10), 1616–1624 (2013).
25. H. L. Butcher, D. Lee, R. Brownsword, D. G. MacLachlan, R. R. Thomson, and D. Weidmann, "Ultrafast laser-inscribed mid-infrared transmission gratings in ig2: modelling and high-resolution spectral characterization," Opt. Express **25**(26), 33617–33628 (2017).
26. A. Grinenko, M. P. MacDonald, C. R. P. Courtney, P. D. Wilcox, C. E. M. Demore, S. Cochran, and B. W. Drinkwater, "Tunable beam shaping with a phased array acousto-optic modulator," Opt. Express **23**(1), 26–32 (2015).
27. R. Content, "Advanced image slicers for integral field spectroscopy with ukirt and gemini," in *Infrared Astronomical Instrumentation*, vol. 3354 (International Society for Optics and Photonics, 1998), pp. 187–200.
28. G. A. Smith, W. Saunders, T. Bridges, V. Churilov, A. Lankshear, J. Dawson, D. Correll, L. Waller, R. Haynes, and G. Frost, "Aaomega: a multipurpose fiber-fed spectrograph for the aat," in *Ground-based Instrumentation for Astronomy*, vol. 5492 (International Society for Optics and Photonics, 2004), pp. 410–420.
29. W. B. Sparks and H. C. Ford, "Imaging Spectroscopy for Extrasolar Planet Detection," Astrophys. J. **578**(1), 543–564 (2002).
30. B. P. Bowler, "Imaging Extrasolar Giant Planets," Publ. Astron. Soc. Pac. **128**(968), 102001 (2016).
31. C. Marois, D. Lafrenière, R. Doyon, B. Macintosh, and D. Nadeau, "Angular Differential Imaging: A Powerful High-Contrast Imaging Technique," Astrophys. J. **641**(1), 556–564 (2006).
32. P. Martinez, M. Kasper, A. Costille, J. Sauvage, K. Dohlen, P. Puget, and J. Beuzit, "Speckle temporal stability in xao coronagraphic images-ii. refine model for quasi-static speckle temporal evolution for vlt/sphere," Astron. Astrophys. **554**, A41 (2013).
33. I. Snellen, R. de Kok, J. Birkby, B. Brandl, M. Brogi, C. Keller, M. Kenworthy, H. Schwarz, and R. Stuik, "Combining high-dispersion spectroscopy with high contrast imaging: Probing rocky planets around our nearest neighbors," Astron. Astrophys. **576**, A59 (2015).
34. T.-O. Husser, S. Wende-von Berg, S. Dreizler, D. Homeier, A. Reiners, T. Barman, and P. H. Hauschildt, "A new extensive library of phoenix stellar atmospheres and synthetic spectra," Astron. Astrophys. **553**, A6 (2013).